International Journal of Impact Engineering 164 (2022) 104202

Contents lists available at ScienceDirect

International Journal of Impact Engineering

journal homepage: www.elsevier.com/locate/ijimpeng

Response of gyroid lattice structures to impact loads

Henrique Ramos [a,b,c,*], Rafael Santiago [a,c], Shwe Soe [d], Peter Theobald [e], Marcílio Alves [b]

[a] Technology Innovation Institute, Material Science Research Centre, Abu Dhabi, United Arab Emirates
[b] Department of Mechatronics and Mechanical Systems Engineering, Group of Solid Mechanics and Structural Impact, University of São Paulo, Brazil
[c] Department of Engineering, Modelling and Applied Social Science, Federal University of ABC, Brazil
[d] Department of Engineering, Design and Mathematics, University of the West of England, United Kingdom
[e] High Value Manufacturing Research, Cardiff School of Engineering, University of Cardiff, United Kingdom

ARTICLE INFO

Keywords:
Additive manufacturing
Finite element analysis
Lattice structure
Impact
Gyroid
AlSi10Mg

ABSTRACT

This paper reports on a comprehensive investigation of gyroid lattice structures subject to impact loading. AlSi10Mg samples were manufactured using selective laser melting (SLM) and mechanically characterized using Digital Image Correlation (DIC). Universal testing machines, drop weight rig, and a split pressure Hopkinson bar were used to mechanically characterize the aluminium alloy at strain rates ranging from, $\dot{\varepsilon} = 10^{-3}$ s^{-1} up to 5500 s^{-1}. Gyroid samples were tested in a drop-weight rig at different impact conditions, where tests results were validated by a FE analysis. These tests, measurements, and analysis enabled the development of a modified gyroid isosurface equation, providing an opportunity to investigate their impact response, where the gyroid wall thickness, unit cell size, and modified isosurface curvature were studied at low-velocity impact conditions. The results indicate that changes in gyroid isosurface topology substantially affect its impact performance.

1. Introduction

Selective laser melting (SLM) is an additive manufacturing (AM) technique that produces metallic components via powder laser bed fusion [1]. A wide range of metallic materials have been studied using SLM process, including stainless steel [2,3], titanium [4,5], copper [6] and aluminium [7–9]. AlSi10Mg is a high-strength aluminum alloy that can be further strengthened by artificial aging. High corrosion resistance [10] is a good material candidate to achieve lightweight components. However, SLM builds exhibit anisotropy [11,12] that influences the mechanical behavior of samples loaded through different orientations [13,14]. Maconachie et al. [15] investigate SLM AlSi10Mg, reporting that components loaded perpendicular to the build direction present higher ductility when compared to other orientations. AM allows the manufacturing of complex geometries directly from a computer-aided design (CAD) model [4,16], providing a new route to achieving high-performance design solutions, here based on lattice structures.

Lattice structures have demonstrated excellent mechanical properties in many engineering applications improving stiffness, strength, toughness, and crashworthiness [17–19]. A gyroid lattice structure is a triple periodic minimal surface (TPMS) with zero mean curvature [20], characterized by minimized local area, where any sufficiently small patch taken from the TPMS has the smallest area among all patches produced under the same boundaries [21]. This structure is formed by smooth and continuous surfaces, infinitely extended in the volume, which divides the space into two congruent inter-twined regions. Shoen [22] was one of the first to study TPMS-gyroid, showing their promising multi-functional structure for a wide range of applications, e.g., impact absorption, heat exchanges, and acoustic management.

Several experimental and numerical studies investigated the mechanical response of the TPMS-gyroid structures. Maskery et al. [20] studied the compressive failure modes and energy absorption of double gyroid structures manufactured using SLM AlSi10Mg. Their results demonstrated the suitability of double gyroid lattices where specific energy absorption under compressive deformation achieves 16×10^6 Jm^{-3} up to 50% strain. Wang et al. [3] investigated 304 stainless steel SLM gyroid lattice structure studying the absorbed energy and deformation modes through quasi-static compression tests. A stable and progressive buckling collapse was observed during compression, while a parametric study indicated that absorbed energy and crushing load were affected by relative density. Yan et al. [2,23] evaluated the mechanical response of gyroid lattice structures under a wide range of volume fractions at different build orientations. Their results indicated that the compression strength of the lattice structures increased with volume

* Advanced Materials Research Center (AMRC) - Technology Innovation Institute, Abu Dhabi, United Arabic Emirates.
E-mail address: henrique.ramos@tii.ae (H. Ramos).

https://doi.org/10.1016/j.ijimpeng.2022.104202
Received 26 July 2021; Received in revised form 2 February 2022; Accepted 15 February 2022
Available online 19 February 2022
0734-743X/© 2022 The Authors. Published by Elsevier Ltd. This is an open access article under the CC BY-NC-ND license (http://creativecommons.org/licenses/by-nc-nd/4.0/).

Table 1
SLM process parameters.

Parameters	Process condition
Average Particle Size	43 μm
Layer Thickness	25 μm
Laser Power	200 W
Hatch Distance	130 μm
Laser Scanning Speed	500 mm/s

fraction. Li et al. [24] conducted a comparison of gyroid structures with different lattices at quasi-static loading Ref. [25]. Their results highlighted that the gyroid lattice structures with the relative density of 20% and 30% absorb more energy per unit mass than the other structures (i.e., Diamond, Gyroid, IWP, and Primitive), indicating the potential application in protective structures. Abueidda et al. [21,26] investigated the uniaxial modulus, compressive strength, and energy absorption of gyroid structures and compared them with different TPMS's such as IWP, Neovius, and Primitive. Their results show that gyroid structures present relatively good mechanical properties, competing well with other lattice structures. These investigations indicate the suitability of gyroid lattice for energy absorbing applications. However, in extreme applications, where materials and structures were subject to high strains and strain rates, like in helmet protective padding and armored panels, the promising application of gyroid lattices demands further investigations given the current paucity of information.

Accordingly, this paper explores the adaptative response of gyroid lattice structures subject to impact loading. The aluminium alloy used to manufacture the gyroid samples were mechanically characterized up to high strain rate levels. An explicit FE model of the gyroid was developed and validated against experimental data. Altogether, the model allows the development of a modified gyroid isosurface. Further, a comprehensive investigation focused on the influence of wall thickness, unit cell size, and the modified equation was conducted to investigate the response of gyroid TPMS's under impact loading.

2. Materials and methods

Aluminum AlSi10Mg alloy was processed using a Renishaw AM250 (Gloucestershire, UK) SLM machine, with the parameters summarized in Table 1. Fig. 1 presents the four standard geometries used for

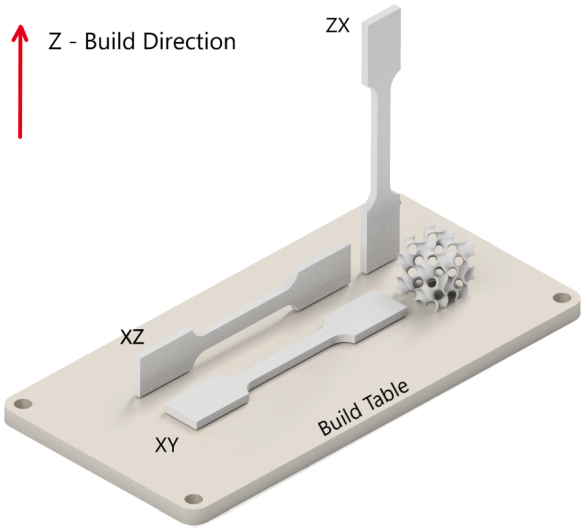

Fig. 2. Part orientation within the build chamber.

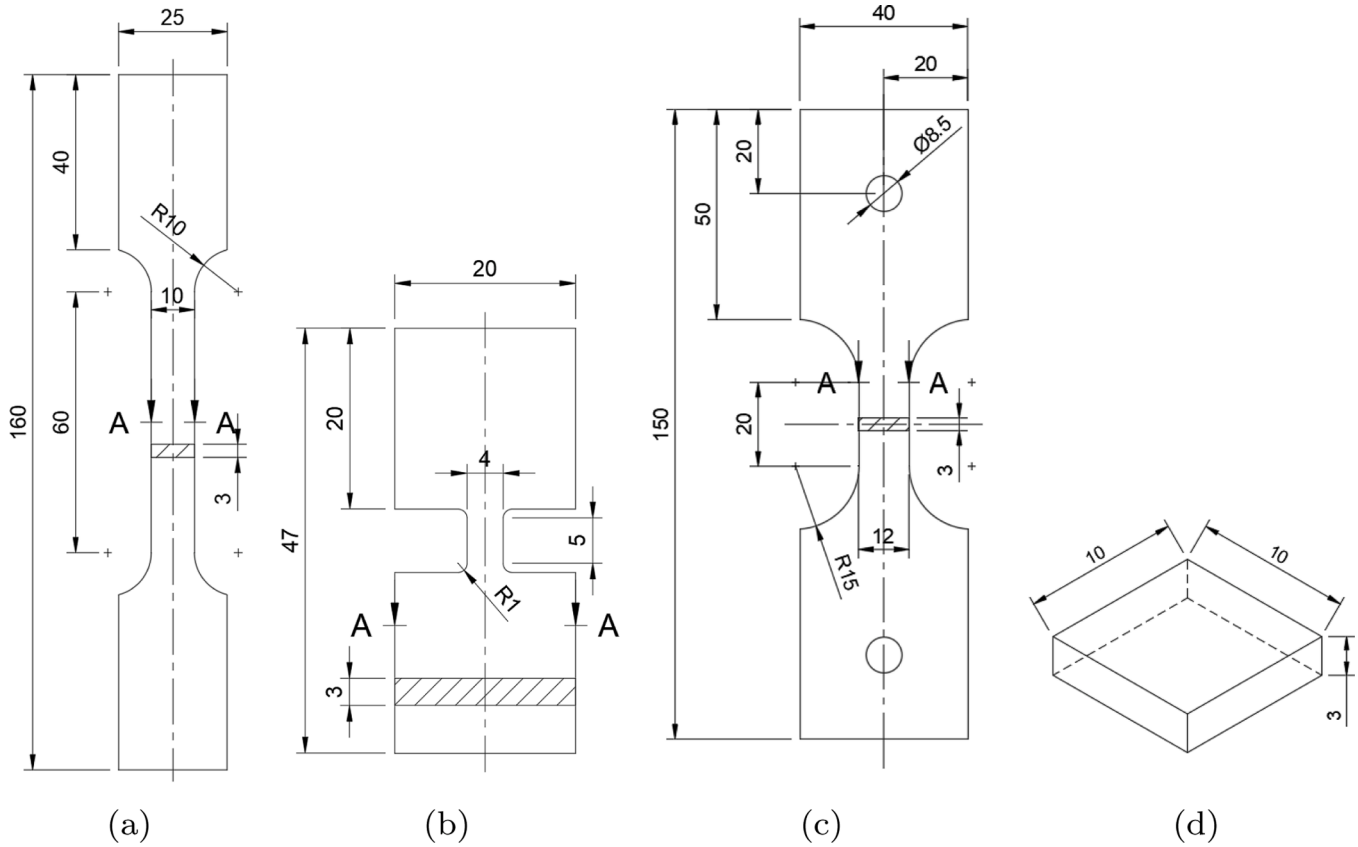

Fig. 1. Specimens used for aluminum AlSi10Mg alloy mechanical characterization: (a) Configuration A, ASTM-E8 Standard [27]; (b) Configuration B; (c) Configuration C; and (d) Configuration D.

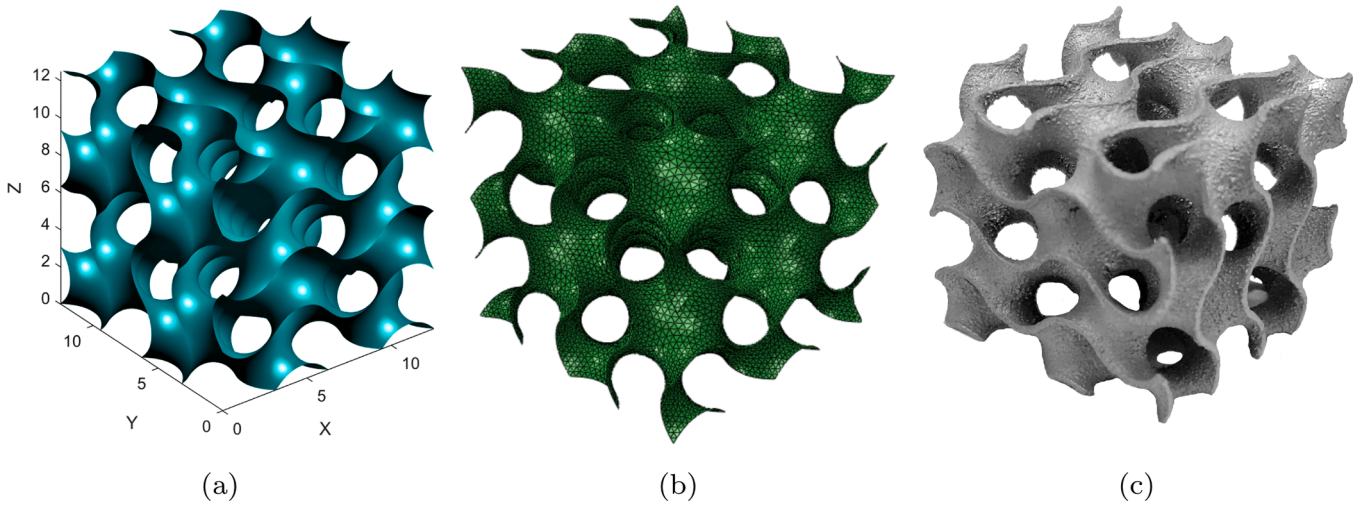

Fig. 3. Gyroid (a) isosurface, (b) FE mesh, and (c) manufactured sample.

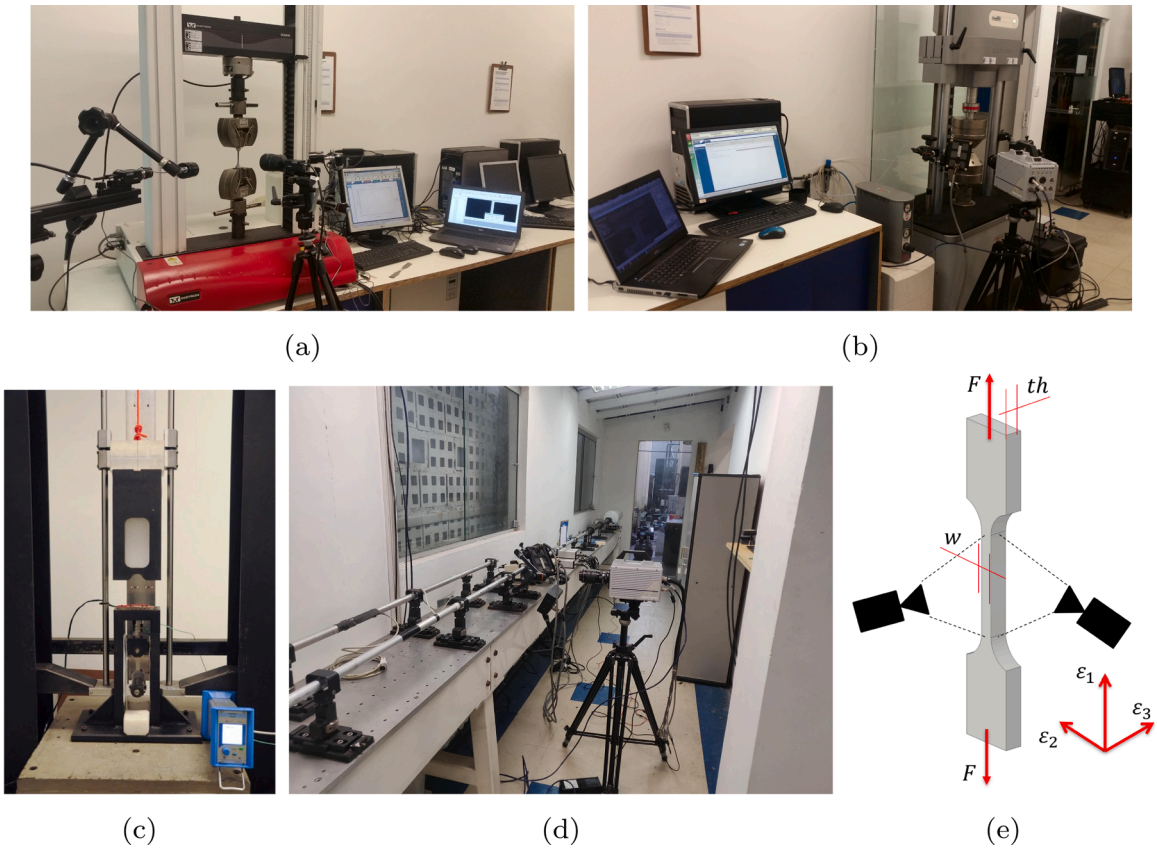

Fig. 4. Equipment used for performing mechanical characterization tests under a wide range of strain rates (a) Instron 3369, (b) Instron EletroPuls E10000, (c) Testing rig that uses the energy of falling mass for performing a tensile test, (d) Split Pressure Hopkinson Bar and (e) specimen local reference used.

mechanical characterization tests at strain rates from 10^{-3} s^{-1} up to 5500 s^{-1}. The specimens were fabricated adopting XY, XZ, and ZX build orientations, as shown in Fig. 2.

The TPMS gyroid isourface, φ_G, is defined by:

$$\varphi_G(x,y,z) = \left[\cos(K_x x)\sin(K_y y) + \cos(K_y y)\sin(K_z z) + \cos(K_z z)\sin(K_x x)\right]^2 - c^2 \tag{1}$$

where c is the gyroid constant, and K_i are the TPMS function periodicities, defined by

$$K_i = 2\pi\frac{n_i}{L_i} \qquad (\text{with } i = x,y,z) \tag{2}$$

n_i are the number of cell repetitions in x, y, z directions, and L_i are the absolute sizes of the structure in each directions [20,22,28]. The gyroid lattice structures isosurface was obtained by implementing Eq. (1) in Matlab (MathWorks, U.S.) software, Fig. 3a. The isosurface was then processed using Hypermesh (Altair Engineering Inc., U.S.) as shown in Fig. 3b, then the lattice thickness was set using MeshMixer (Autodesk,

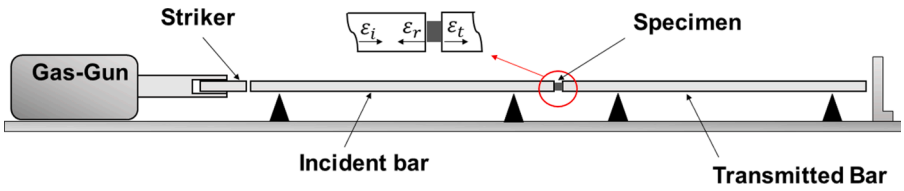

Fig. 5. Schematic of the Split Pressure Hopkinson Bar used for the high strain rate tests.

Inc., U.S.). Finally, the CAD file was generated and imported to Renishaw QuantAM build preparation software. The gyroid samples were 30 mm × 30 mm × 30 mm, where each cell being 7.5 mm × 7.5 mm × 7.5 mm (i.e., 4 cells in each direction, 64 cells in all), Fig. 3c. The samples have a wall thickness of 0.75 mm, presenting a relative density of $\rho_{rel} = 14.3\%$, which is the ratio of the lattice structure density to the monolithic material density.

2.1. Mechanical characterization

Mechanical properties were obtained from uniaxial tests, using a universal testing machine, Instron 3369 ($\dot{\varepsilon} = 10^{-3}$ s^{-1}), an electro-mechanical device ElectroPuls E10000 ($\dot{\varepsilon} = 10$ s^{-1}), a designed rig that uses a dropped mass to generate high strain-rates ($\dot{\varepsilon} = 350$ s^{-1}) [29], and a Split Pressure Hopkinson Bar, i.e. SPHB ($\dot{\varepsilon} = 5500$ s^{-1}) [30], Fig. 4a–d. This strain rate range encompasses a wide strain rate interval.

Full-field deformation was measured using an optical measurement technique based on digital image correlation (DIC), recorded by two 5.0 megapixels cameras or a high-speed camera, for the quasi-static and dynamic tests, respectively. For the quasi-static tests ($\dot{\varepsilon} = 10^{-3}$ s^{-1}), the cameras were synchronized, one covering the specimen frontal face (1 and 2 plane) and another covering the specimen thickness (1–3 plane) (Fig. 4e). The samples were painted in white before application of black speckled pattern, enabling surface-based strain analysis (VIC-2D, Correlated Solutions, U.S.). This enables measurement of the specimen cross-section and calculation of the Lagrangean strain on the specimen surface. Thus, from,

$$\sigma = \frac{F}{t_h.w(1+\varepsilon_2)(1+\varepsilon_3)}, \tag{3}$$

where t_h and w being the specimen thickness and width, respectively. Strain ε_2 and ε_3 are obtained from DIC, Fig. 4e, and the force,F, recorded from the universal testing machine load cell.

For the dynamic tests, a high-speed camera, at a rate of 5k frames per second, synchronized to the data acquisition board, recorded the specimen frontal face (1 and 2 plane) so the obtained stress is

$$\sigma = \frac{F}{t_h.w(1+\varepsilon_2)} \tag{4}$$

The SPHB technique, Fig. 5, was used to identify the material response at a high strain rate, with samples positioned between two cylindrical bars (incident and transmitted bar). During the test, a striker bar is accelerated by a gas gun impacting the incident bar, inducing an elastic pulse that travels along the incident bar, $\varepsilon_i(t)$, until the opposite bar end. The pulse is partially reflected, $\varepsilon_r(t)$, and partially transmitted, $\varepsilon_t(t)$. These strain pulses are recorded by strain gauges installed on the bars so that the specimen stress, strain, and strain rate are [31],

$$\varepsilon_i(t) = \varepsilon_t(t) - \varepsilon_r(t) \tag{5}$$

$$\sigma(t) = E_B \frac{A_B}{A_s} \varepsilon_t(t) \tag{6}$$

$$\varepsilon_s(t) = \frac{2C_0}{l_s} \int_0^t \varepsilon_r(t) dt \tag{7}$$

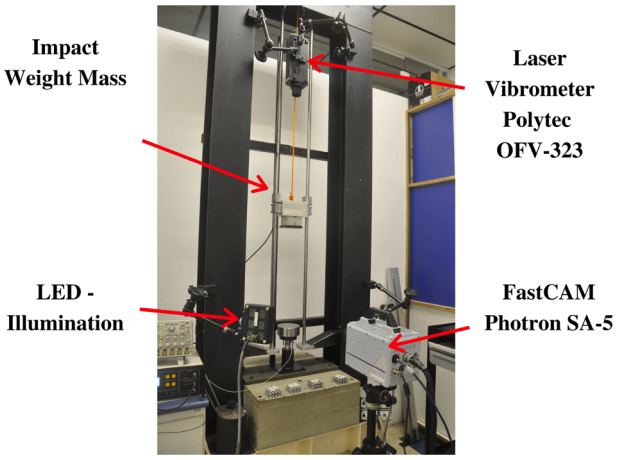

Fig. 6. Low-velocity impact rig.

$$\dot{\varepsilon}_s(t) = \frac{2C_0}{l_s} \varepsilon_r(t) \tag{8}$$

2.2. Microstructure characterization

Scanning Electron Microscope (SEM) analysis was conducted on the printed specimens. Coupons were prepared to examine their microstructure by a dual-beam electron microscope Quanta 3D FEG (FEI inc., U.S.).

2.3. Impact test

Gyroid samples were tested in a drop-weight rig, as presented in Fig. 6. Velocity history was measured using a laser vibrometer OFV-323 (Polytec GmbH), with the output voltage signal recorded using a NI PCI-6110 (National Instruments, U.S.) at 500 k samples/s. A Photron SA5 (Imagina Group Inc., Japan) high-speed camera was also used at the rate of 3k fps for qualitative comparison with numerical results. Data analysis was conducted by comparing impact velocity (V_{imp}), residual velocity (V_{res}), maximum displacement (δ_{max}), peak load (F_{max}) and the absorbed energy (S),

$$S = \int_{L_0}^{L_1} F \, dL \tag{9}$$

where F is the impact load and L_0 and L_1 are the initial and final gyroid heights, respectively. The impact force and compressive displacement were derived from the velocity data recorded by the laser vibrometer.

2.4. Numerical model

In order to predict the deformation behavior and mechanical properties of the gyroid lattice structure, the finite element analysis was carried out using Abaqus dynamic explicit code (Dassault Systèmes, France). The lattices surfaces were meshed using 4-node shell elements, with reduced integration and large-strain formulation (*S4R* elements).

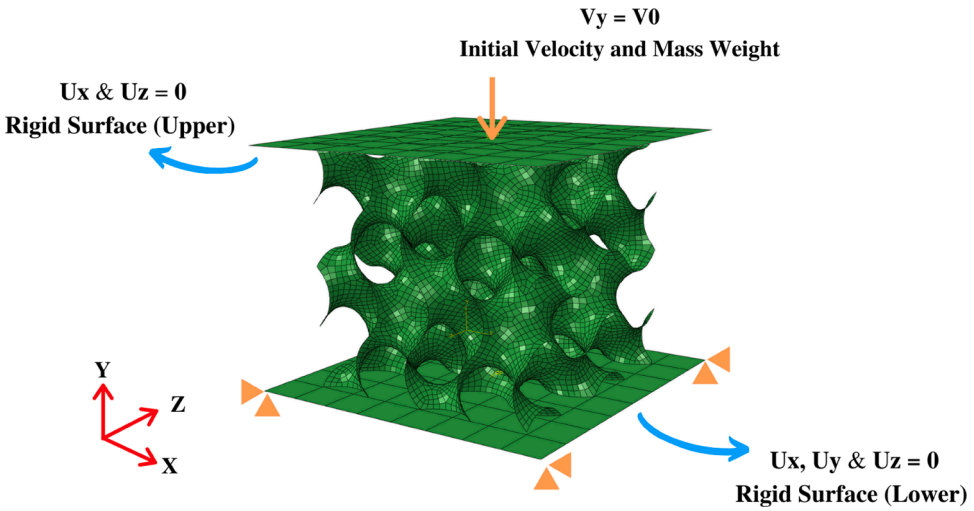

Fig. 7. Model of gyroid 4 × 4 × 4 cell lattice with boundary conditions.

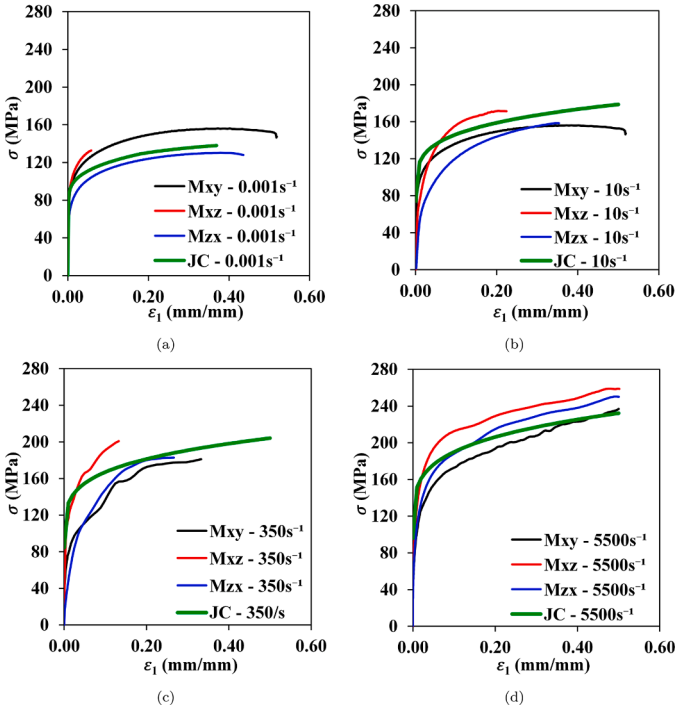

Fig. 8. (a) The influence of the build orientation in the material strain-stress response for quasi-static strain-rate of $\dot{\varepsilon} = 10^{-3}$ s^{-1}. Single homogenized FE and experimental comparison of the AlSi10Mg allo. (b) The influence of the strain-rate in AlSi10Mg aluminum alloy strain-stress response in different build orientations with FE and experimental comparison for the strain-rate of 10 s^{-1}, (c) 350 s^{-1}, and (d) 5500 s^{-1}.

Convergence analysis based on mesh sensitivity was performed, leading to 0.75 mm of element size as the best compromise between processing time and result convergence. In this model, the shell elements are defined to have a normal contact behavior using hard contact formulation, and a friction coefficient of 0.2 for the tangential response [32]. The lower gyroid face was placed on a rigid surface, and the upper face was impacted by a moveable rigid block with a defined mass and initial velocity, as shown in Fig. 7. The central point of the upper plate and the lower surface were used to obtain the displacement and force, respectively.

Table 2
Strain-rate effects on aluminum alloy AlSi10Mg. E is the Young modulus, σ_0 is the yield stress, σ_u is ultimate stress, ϵ_u is ultimate strain, and ν_e is the Poisson ratio $\nu_e = \varepsilon_2/\varepsilon_3$.

Strain rate (s^{-1})	Build direction	E (GPa)	σ_0 (MPa)	σ_u (MPa)	ε_u (mm/mm)	ν_e (mm/mm)
0.001	XY	38.8	67.5	156.6	0.51	0.29
0.001	XZ	40.7	68.8	132.7	0.05	0.45
0.001	ZX	38.9	60.1	125.9	0.37	0.38
10	XY	–	69.6	174.6	0.36	0.30
10	XZ	–	72.8	158.3	0.35	0.34
10	ZX	–	69.3	140.86	0.18	0.36
350	XY	–	82.8	175.8	0.48	0.35
350	XZ	–	93.2	200.8	0.13	0.43
350	ZX	–	85.8	178.1	0.49	0.39
5500	XY	–	103.5	241.9	0.50	–
5500	XZ	–	112.7	258.7	0.50	–
5500	ZX	–	108.2	250.2	0.50	–

3. Results and discussion

3.1. Material characterization

It was noted that all tensile samples failed within the effective gauge length, the region where the strain data were taken for DIC analysis. Fig. 8a compares the influence of the build direction in the material response for the quasi-static strain rate. Experimental data indicates that the samples presented an elastic-plastic anisotropic behavior, where specimens manufactured in the XZ direction showed lower strength and ductility, exhibiting a more brittle response. Clearly, the scanning strategy and build orientation influence the specimen mechanical response, leading the material to a brittle premature failure. The XZ and XY build orientation differed due to the relatively small areas deposited during each melting process. On the contrary, XY specimens manufacturing was quicker given the number of powder layers and high thermal gradient cycles, resulting in a ductile stress-strain response.

Dynamic response of the aluminum alloy was evaluated at strain rates around 10 s^{-1}, 350 s^{-1}, and 5500 s^{-1}, Fig. 8b–d. Experimental data at 10 s^{-1} and 350 s^{-1} present similar behavior as the quasi-static strain rate, whose samples in the XZ direction show a more brittle premature failure response. For the high strain rate tests at the SPHB, strain is limited to 50%. Stress values presented an increase when subject to higher strain-rate levels for all built orientations. Indeed, an increase of approximately 53% on the stress response for the higher strain-rate value ($\dot{\varepsilon} = 5500$ s^{-1}), was found by comparing to the quasi-static

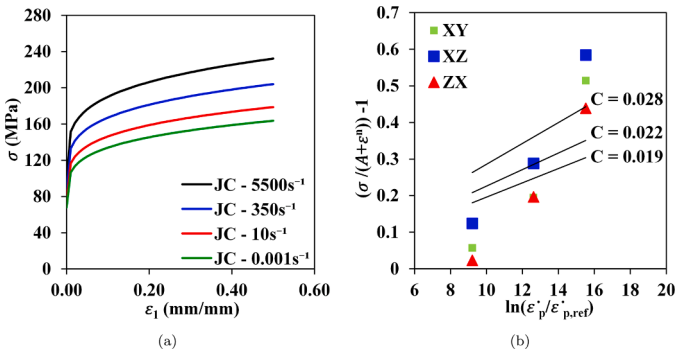

Fig. 9. (a) Homogenized Stress-strain response of JC parameter for all strain rates studied (b) Natural logarithm of strain rate and stress at $\varepsilon_p = 0.3$ with linear trendlines and correlations.

Table 3
Material constitutive parameters implemented in the numerical models.

Aluminum alloy AlSi10Mg		
Parameter	Description	Value
E	Elastic modulus	39.46 GPa
ρ	Density	2.78×10^{-9} ton/mm^3
ν	Poisson ratio	0.37
A	JC constitutive parameter	65.46 MPa
B	JC constitutive parameter	122.05 MPa
n	JC constitutive parameter	0.30
C	JC constitutive parameter	0.023
D_1	Damage JC parameter	− 0.020
D_2	Damage JC parameter	0.130
D_3	Damage JC parameter	− 1.150
D_4	Damage JC parameter	0.011

material response ($\dot{\varepsilon} = 10^{-3}$ s^{-1}). Table 2 summarizes the mechanical properties of aluminum AlSi10Mg alloy made by SLM.

Material behavior was modeled by the *Johnson–Cook* (JC) constitutive law [31,33,34], with the plastic stress, σ_p expressed as a function of the plastic strain, ε_p, strain-rate, $\dot{\varepsilon_p}$, and quasi-static strain rate, $\dot{\varepsilon}_{p,ref}$, according to,

$$\sigma_p = \left[A + B(\varepsilon_p)^n\right]\left[1 + C\ln\left(\frac{\dot{\varepsilon_p}}{\dot{\varepsilon}_{p,ref}}\right)\right] \quad (10)$$

with possible temperature effects being disregarded. A, B, n, and C are material constants derived from the experimental data by a nonlinear regression using a subroutine implemented in Matlab (MathWorks, U. S.). The results for regression analysis on quasi-static tensile data were used to identify yield and plasticity parameters for each build orientation. The JC strain rate parameter was extracted considering a value of $\varepsilon_p = 0.3$ compressive strain. Fig. 9 shows the JC prediction of strain-rate effect for the aluminum alloy in a wide range of strain rates. The strain hardening effect is observed at the selected plastic deformation for all build directions. Fig. 8b–d presents the homogenized curve using the linear strain rate sensitivity of the flow stress at selected strain within 10^{-3} s^{-1} and 5500 s^{-1} strain rate, where the stress-strain response showed a good dynamic agreement between the numerical prediction and experimental data. Damage parameters, to be used later, were extracted from the literature [35], and assumed to be valid for the present alloy. Minor adjustments are applied to improve the agreement to experimental data. The single homogenized set of constitutive parameters normalized from all the directions tested is listed in Table 3.

3.2. Impact results and numerical validations

Experimental data of the gyroid tests are summarized in Figs. 10–12 and Table 4. Note that a homogeneous compressive deformation through the lattices height was observed in all samples studied cases. No visible material failures were noted at any impact energy level. The force-displacement responses are presented in Fig. 13, in which a typical cellular solid behavior was observed under compression, i.e., initial linear loading followed by a plateau region and densification at high deformation levels (*M*5 and *M*6). After impact, a spring-back response was also noted, being the plateau load consistent for all samples.

Due to the complex process of AM, defects can also be inevitably in the manufacturing parts. A scanning electron microscope (SEM) was used to microphotograph the SLM printed gyroid specimen. Fig. 14 shows the specimen surface unmelted powder, porosity, and voids. In Fig. 14a an inhomogenous gyroid wall thickness can also be found, which is likely to induce stress concentration leading to a brittle failure

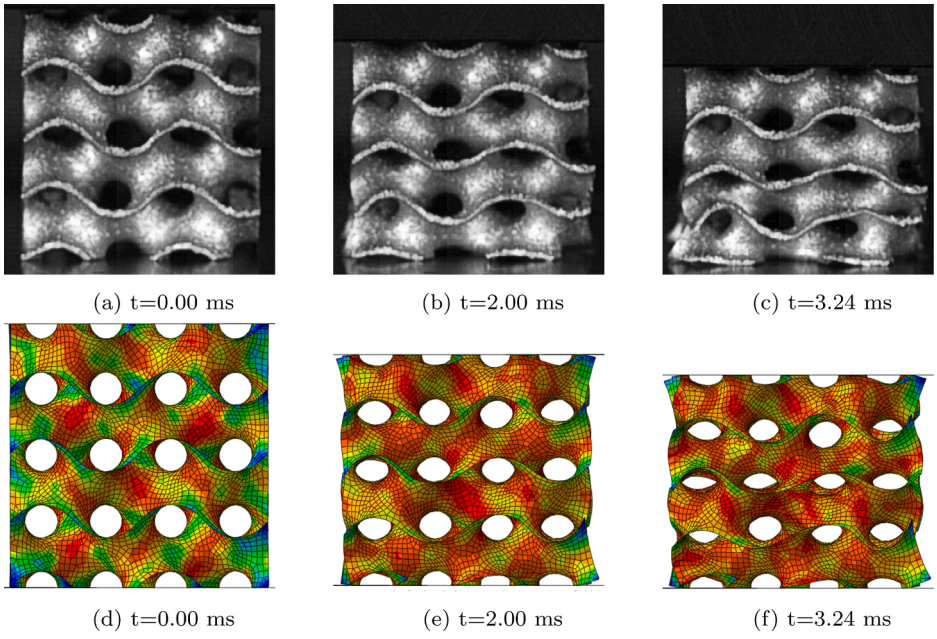

Fig. 10. Qualitative comparison of gyroid response during (a) experimental impact test and (b) FEA at impact conditions of 4.0 m/s and 4.8 kg.

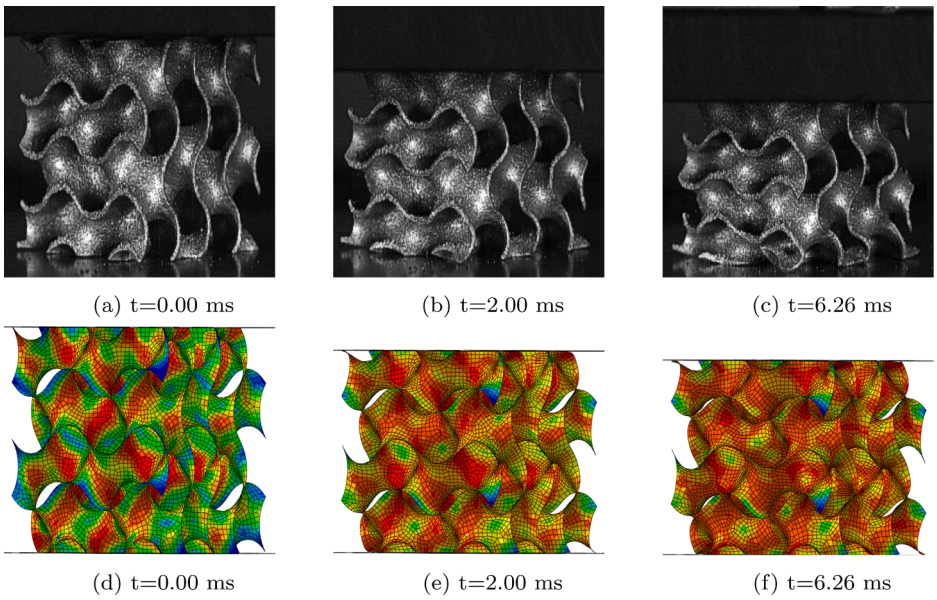

Fig. 11. Qualitative comparison of gyroid response during (a) experimental impact test and (b) FEA at impact conditions of 2.0 m/s and 14.8 kg.

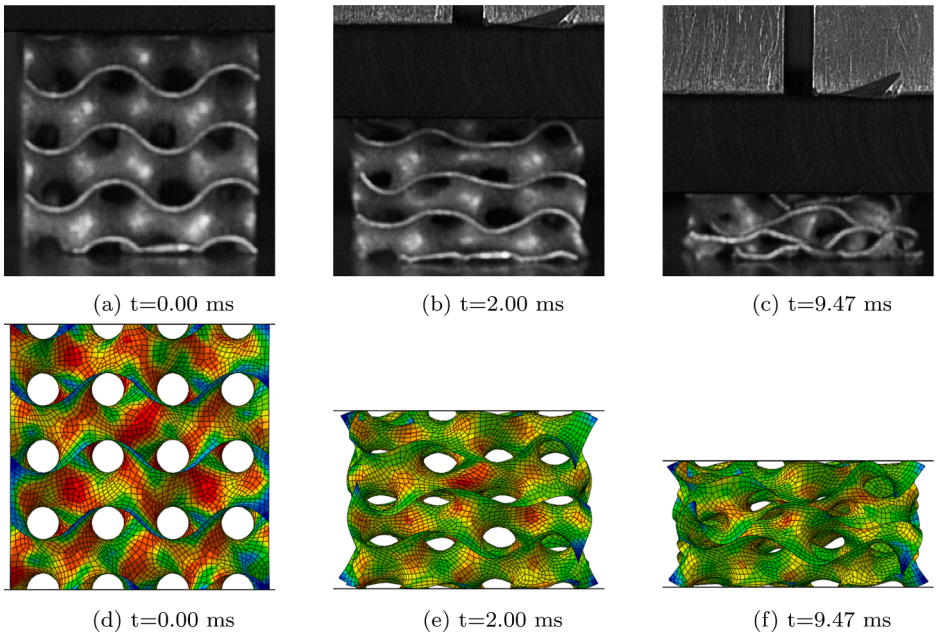

Fig. 12. Qualitative comparison of gyroid response during (a) experimental impact test and (b) FE at impact conditions of 4.0 m/s and 14.8 kg.

Table 4
Summary of experimental gyroid lattice structure under impact condition.

Specimen	Impact mass (Kg)	V_{inc} (m/s)	E_{inc} (J)	V_{res} (m/s)	δ_{max} (mm)	F_{max} (kN)	S (J)	S/E_{inc} (%)	S_{esp} (S/ρ_{rel}) (J)
M1	4.80	4.18	41.93	0.46	6.12	8.56	40.97	97.71	286.50
M2	4.80	4.26	44.16	0.41	6.29	7.66	40.20	91.03	281.11
M3	14.80	2.34	40.51	0.35	5.57	11.39	39.53	97.58	276.43
M4	14.80	2.35	40.86	0.34	6.00	16.24	39.91	97.67	279.09
M5	14.80	4.03	120.18	0.31	15.08	13.24	117.56	97.81	822.09
M6	14.80	4.09	123.78	0.38	18.49	12.01	122.68	99.11	857.90

[36,37]. The visible fluctuations in the experimental impact response of gyroid structures are possibly caused by the poor ductility of ALSi10Mg due to manufacturing imperfections as observed by SEM images. This is described by Gibson and Ashby [38], with the brittle failure of materials leading to fluctuations in the lattice structure compressive response. Several authors also observed these fluctuations in the compressive response of TPMS lattice structures [24,37,39,40]. These pre-existing defects can be served as cracks initiation sites, resulting in the low-strain to fracture the gyroid shell. Besides, it is challenging to locate the crack initiation site due to the complexity of gyroid topology. Some

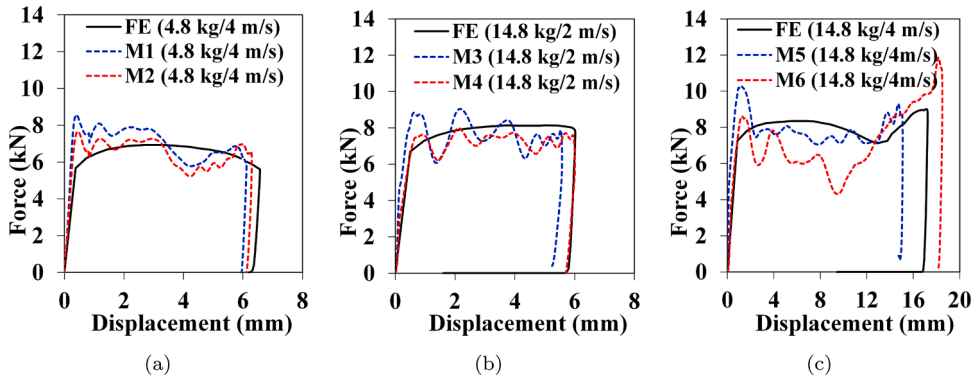

Fig. 13. Force-displacement response of (a) M1-M2, (b) M3-M4 and (c)M5-M6 gyroid lattices and comparison between experimental impact and FE analysis.

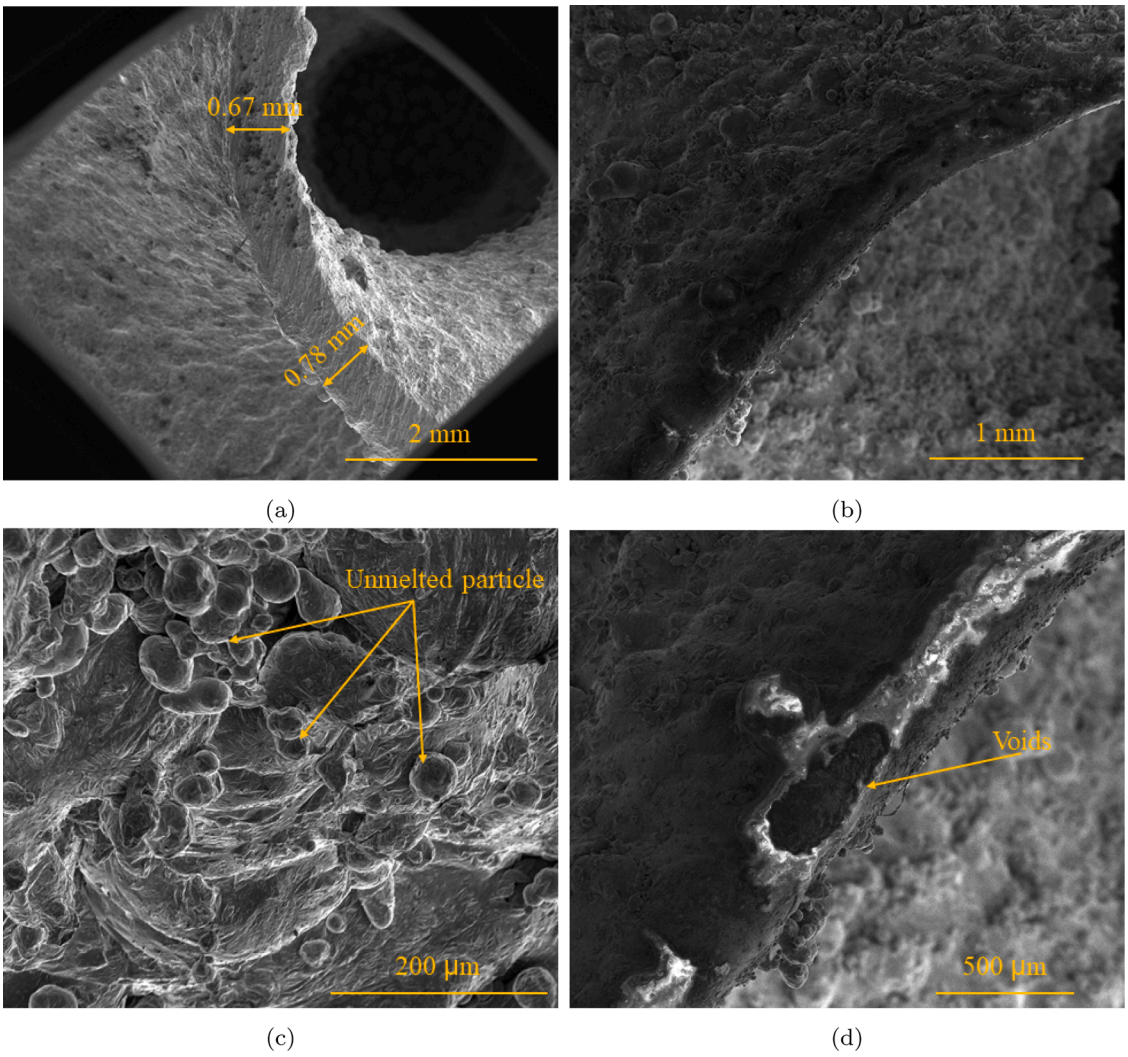

Fig. 14. Scanning electron microscope observed surface morphology of the SLM gyroid lattice structure.

authors highlighted that these fluctuations could be overcome by heat treatment [7,20,41–43].

The drop weight test and simulation results are depicted in Fig. 13. The results predicted well the overall behavior of the gyroid structures, capturing different stages in the compressive force-displacement response. Some deviations between numerical and experimental results can be identified. The initial peak force of experimental results is generally higher than the numerical predictions. This may be caused by geometric deviations between the mathematical curves, and the actual models manufactured samples [37]. The numerical prediction also does not capture force fluctuations well since the FE model is not constructed to consider possible thickness variations and pre-existing defects. These localized defects (Fig. 14) are subject to local buckling and fracture, resulting in a strength loss not predicted by the homogeneous FEM (Table 5).

Table 5
Quantitative results comparison between experimental results and numerical models.

Specimen identification	V_{inc} (m/s)	V_{res} (m/s)	δ_{max} (mm)	F_{max} (kN)	S (J)	S_{esp} (S/ρ_{rel})(J)
			4.8 kg and 4 m/s			
Experimental	4.22 ± 0.04	0.43 ± 0.02	6.20 ± 0.08	8.11 ± 0.45	40.58 ± 0.38	283.80 ± 2.69
Numerical	4.21	0.48	6.57	6.92	39.72	277.76
Deviation	–	11.32%	5.96%	14.67%	2.11%	2.15%
			14.8 kg and 2 m/s			
Experimental	2.14 ± 0.01	0.34 ± 0.01	5.78 ± 0.21	13.81 ± 2.42	39.72 ± 0.19	277.73 ± 1.30
Numerical	2.14	0.37	5.74	7.42	44.50	311.18
Deviation	–	4.41%	0.69%	46.27%	12.03%	12.04%
			14.8 kg and 4 m/s			
Experimental	4.06 ± 0.03	0.34 ± 0.03	16.78 ± 1.70	12.62 ± 0.61	120.12 ± 2.56	839.99 ± 17.90
Numerical	4.06	0.34	16.86	8.16	130.43	912.03
Deviation	–	1.44%	0.44%	35.36%	8.58%	8.57%

3.3. Gyroid impact response

The impact response of the gyroid structure was carried out numerically by comparing different topologies, subject to 14.8 kg impact mass at 2.3 m/s (39.14 J). A 30 mm × 30 mm × 30 mm gyroid lattice was designed and numerically modeled using different wall thicknesses, unit cell sizes, and isosurface tunings. The peak force, maximum displacement, and absorbed energy were obtained from the force-displacement responses.

To analyze how the unit cell size influences the gyroid impact response, the lattices were designed with unit cells ranging from 5 mm (216 units cells) to 15 mm (8 unit cells), as summarized in Table 6, with 0.80 mm wall thickness in all cases. The influence of wall thickness was explored by modeling a 64-unit cell gyroid with (7.5 mm cell size), with wall thicknesses varying from 0.5 mm to 1.5 mm, as summarized in Table 7.

Fig. 15 a shows the force-displacement response for the different cell sizes of Table 6. All configurations absorbed a similar amount of energy. However, as the number of unit cells increases (smaller unit cells), the peak force (F_{max}) increases, and maximum residual displacement (δ_{max}) reduces. On the contrary, as the number of unit cells decreases (larger unit cells), the peak force (F_{max}) decreases, and maximum residual displacement (δ_{max}) increases. The relative density changes with the number of cell sizes. Thus, when the lattice relative density is considered, larger unit cells minimize δ_{max}/ρ_{rel}, which indicates better performance. Smaller unit cells tend to minimize F_{max}/ρ_{rel} ratio, suggesting a better performance since the peak force, i.e., maximum acceleration, reduces.

Fig. 15 b summarizes the force-displacement curves for gyroids with different wall thicknesses, also summarized in Table 7. The energy absorbed is similar for all cases, increasing slightly for thicker lattices. The residual displacement increases for thinner lattices as the peak force decreases. Considering the relative density, thinner gyroids exhibit a more favourable δ_{max}/ρ_{rel} ratio, whilst thicker lattices demonstrate higher F_{max}/ρ_{rel} ratio. The wall thickness increase is comparable to an enlargement of unit cells (less amount of unit cells), whilst a reduction of the wall thickness is similar to smaller unit cells gyroids (less amount of unit cells) in terms of the gyroid response during impact events. Thicker walls minimizes δ_{max}/ρ_{rel}, and thinner walls tend to minimize the F_{max}/ρ_{rel} ratio.

To evaluate the influence of minor tunes in the gyroid topology, the parameters α_1, α_2 and α_3 were implemented to the gyroid isosurface equation, according to

$$\varphi_G(x,y,z) = \left[\alpha_1\cos(K_x x)\sin(K_y y) + \alpha_2\cos(K_y y)\sin(K_z z) + \alpha_3\cos(K_z z)\sin(K_x x)\right]^2 - c^2 \quad (11)$$

These parameters allow smoothing of the gyroid topology whilst retaining its relative density, as summarized in Table 8. The α_n parameters were set to 0.8, 1.0, and 1.3 in all possible combinations. Table 9

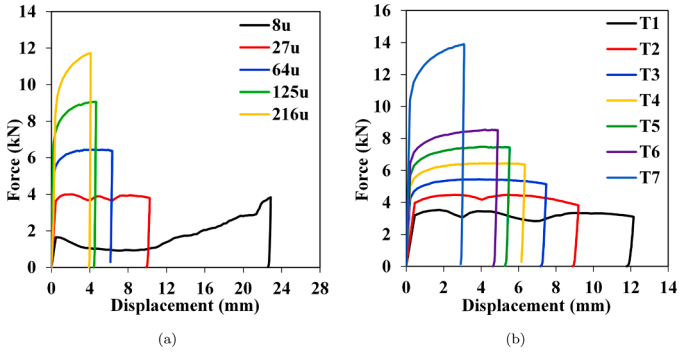

Fig. 15. (a) Influence of cell size and (b) wall thickness on the gyroid impact response.

Table 6
Summary of gyroid structures with different unit cells and their respective influence on impact response.

Specimen identification	ρ_{rel} (%)	Overall size (mm)	Wall thickness (mm)	Cell size (mm)	δ_{max} (mm)	F_{max} (kN)	S (J)
8u	8.64	30 × 30 × 30	0.80	15.00	22.86	3.83	38.65
27u	13.03			10.00	10.25	3.99	38.19
64u	17.40			7.50	6.34	6.44	38.38
125u	21.75			6.00	4.65	9.03	38.75
216u	25.39			5.00	4.08	11.72	38.18

Table 7
Summary of gyroid structures with different wall thicknesses and their respective influence on impact response.

Specimen identification	ρ_{rel} (%)	Overall size (mm)	Cell size (mm)	Wall thickness (mm)	δ_{max} (mm)	F_{max} (kN)	S (J)
T1	10.86	30 × 30 × 30	4 × 4 × 4	0.50	12.15	3.52	38.30
T2	13.02			0.60	9.21	4.46	38.16
T3	15.05			0.70	7.48	5.44	38.45
T4	17.40			0.80	6.34	6.44	38.38
T5	19.50			0.90	5.52	7.47	38.27
T6	21.60			1.00	4.89	8.55	38.17
T7	32.55			1.50	3.10	13.89	37.69

Table 8
Summary of gyroid isosurface equation tuned by α_n and their respective influence on impact response.

Gyroid	α_1	α_2	α_3	ρ_{rel} (%)	Overall size (mm)	Wall thickness (mm)	δ_{max} (mm)	F_{max} (kN)	S (J)
BL	1.0	1.0	1.0	17.40	30 × 30 × 30	0.80	6.34	6.44	38.38
1H	1.3	1.0	1.0				6.54	6.30	38.39
1L	0.8	1.0	1.0				6.66	6.14	38.41
2H	1.0	1.3	1.0				6.78	6.06	38.33
2L	1.0	0.8	1.0				6.10	6.68	38.41
3H	1.0	1.0	1.3				5.82	7.00	38.39
3L	1.0	1.0	0.8				6.68	6.18	38.30
12H	1.3	1.3	1.0				6.83	6.04	38.30
12L	0.8	0.8	1.0				5.94	6.87	38.43
13H	1.3	1.0	1.3				6.05	6.74	38.39
13L	0.8	1.0	0.8				6.66	6.14	38.32
23H	1.0	1.3	1.3				6.21	6.55	38.24
23L	1.0	0.8	0.8				6.38	6.61	38.34
12L 3H	0.8	0.8	1.3				5.39	7.58	38.45
12H 3L	1.3	1.3	0.8				7.15	5.81	38.23

Table 9
Example of tuned gyroid topologies for $\alpha_1 = 0.8$, 1.0, and 1.3.

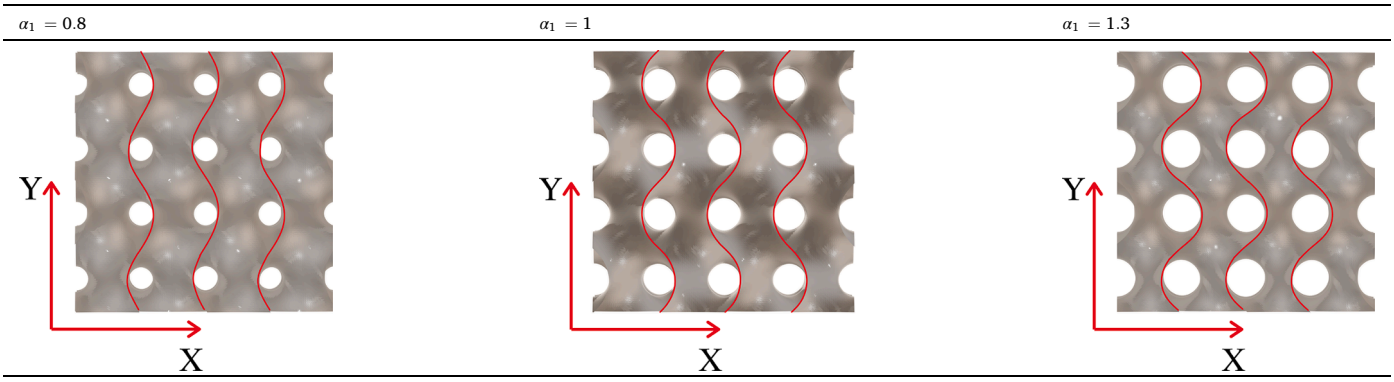

exemplifies the influence of α_1 parameter in the gyroid isosurface. As α_1 changes, so do the height of the gyroid cell in the XY plane. The same pattern was also observed for α_2 and α_3 values, in *YZ* and ZX planes, respectively.

Table 8 and Fig. 16 summarize the impact response of the gyroids with the α_n variation. The α_n combinations influence the force-displacement response of the gyroid during the impact event when compared to the baseline gyroid topology. Fig. 17 highlights that the α_3 exhibits major response changes when compared to the baseline isosurface. In this case, the modified isosurface in the XZ plane changes the lattice surface curvature perpendicular to the loading direction. Hence, 3*H* configurations present larger cells in XZ planes, which results in a more stretching dominant load in the lattices walls, leading to a higher force.

Fig. 16 d - 16 f show the gyroid impact response when a pair of α_n parameters are changed. In those cases, the parameters influenced the force-displacement response of gyroid during the impact, with the $\alpha_1 - \alpha_2$ combination exhibiting a greater influence. It is noted that those parameters mainly change the cell sizes in XY and *YZ* planes, which are both aligned to the loading direction.

Finally, it was shown that the proposed parameters α_n are effective for optimizing the gyroid impact response. Those parameters can modify the peak force and maximum displacement, with no relative density and absorbed energy changes. For example, using a gyroid with higher α_1 and α_2, and lower α_3 (e.g., 12*H* 3*L*) could be suitable for motorcyclist helmet protective padding [44]. Such combination leads to minor peak force, consequently minimizing the acceleration and traumatic brain injury severity during falls or collisions. Another application, using gyroid lattices with lower α_1 and α_2, and higher α_3 (e.g., 12*L* 3*H*) that minimize the maximum displacement, could be suitable for personal armour protective clothing [45], once the penetration resistance requires tailored structure to mitigate the backface signature interface. This indicates that gyroid-based lattices could be particularly advantageous in applications that require an engineered compressive response, e.g., aerospace, automotive, and personal protection applications. In addition, the parameters α_1, α_2 and α_3 can easily be implemented in the design-of-experiment sub-routine to optimize their response accordingly.

4. Conclusions

The compressive behavior of AlSi10Mg gyroid lattice structures was investigated under low-velocity impact loading. Finite element analysis was conducted to validate the deformation evolution in the tested configurations under low-velocity impact. A novel gyroid isosurface was developed where parameters implemented to the isosurface equation lead to a change in the force-displacement impact response with no influence on its relative density. The following conclusions can be drawn:

- AlSi10Mg was mechanically characterized at different loading directions subject to nominal strain rates ranging from 10^{-3} s^{-1} up to 5500 s^{-1}. The DIC technique was adopted to extract the mechanical properties where the Johnson–Cook constitutive parameters were defined. The aluminum alloy was shown to be strain rate and build orientation sensitive.
- SEM results indicate some printing imperfections and unmelted powders on the gyroid specimen surfaces. Finite element analysis provides an overall agreement on the deformation evolution. The numerical prediction did not capture force fluctuations, whereas the FEM does not take thickness variations and pre-existing defects into the model.

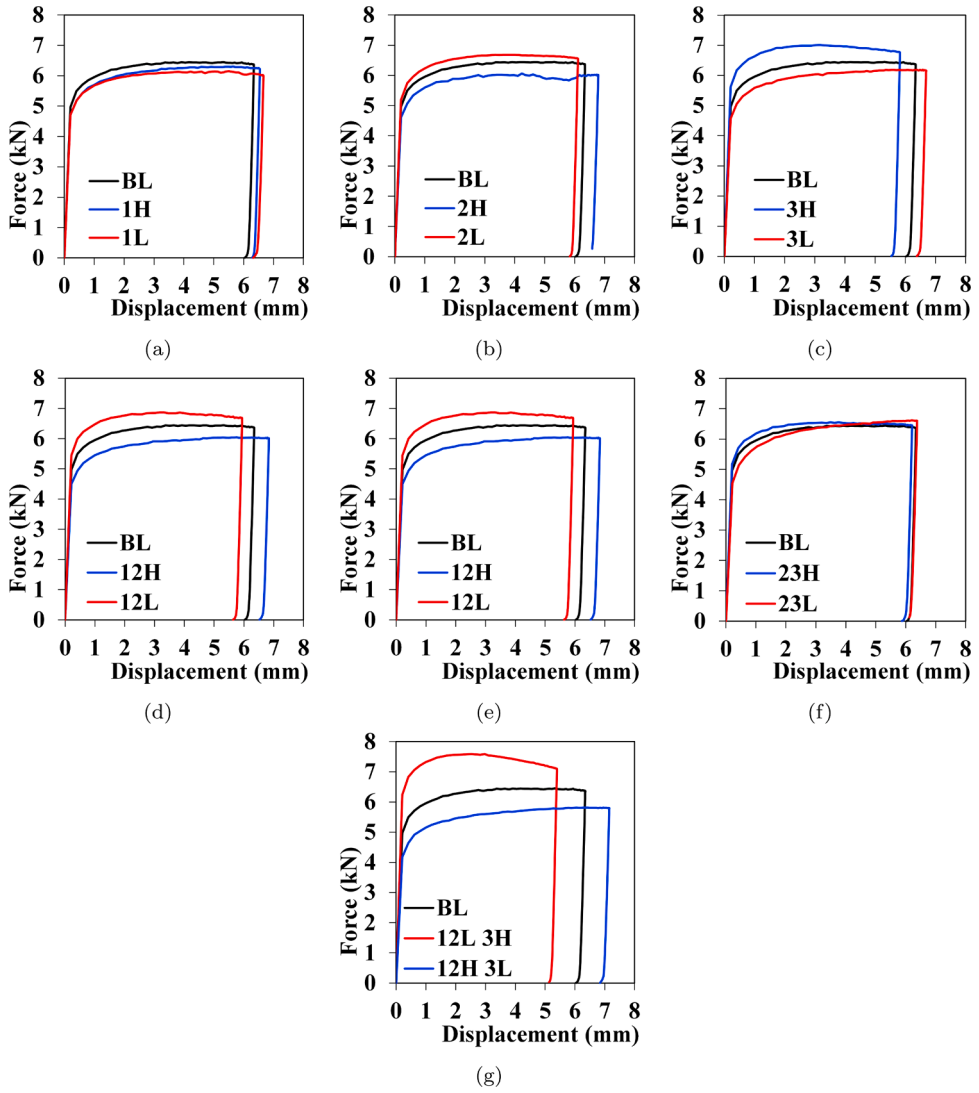

Fig. 16. Influence of the modified isosurface gyroid equation on the impact response of the gyroid in comparison with the gyroid baseline.

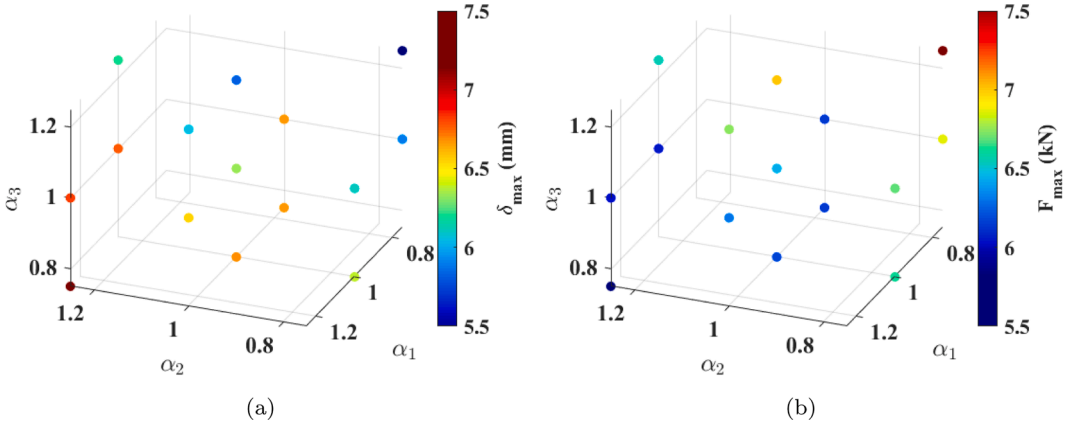

Fig. 17. Maximum displacement (a) and Peak Force (b) impact response according with the influences of $\alpha_1 - \alpha_2$ in the modified isosurface gyroid equation.

- The modified gyroid equation shows that the α_n parameter proposed can change the deformation behavior of gyroid lattice structures under low-velocity impact loading. Changes in the peak force and maximum displacement with no change in the relative density or energy absorption can be observed in the numerical evaluation. The parameters α_1, α_2 and α_3 can easily be implemented in the design-of-experiment sub-routine to optimize the impact response accordingly with the desired engineering application.

CRediT authorship contribution statement

Henrique Ramos: Methodology, Validation, Investigation, Formal analysis, Writing – original draft, Writing – review & editing. **Rafael Santiago:** Conceptualization, Investigation, Writing – review & editing, Supervision. **Shwe Soe:** Resources, Writing – review & editing. **Peter Theobald:** Resources, Writing – review & editing, Funding acquisition. **Marcílio Alves:** Formal analysis, Resources, Writing – review & editing.

Declaration of Competing Interest

The authors declare that they have no known competing financial interests or personal relationships that could have appeared to influence the work reported in this paper.

Acknowledgment

The authors would like to express their thanks and appreciation to Natalia Ghisi in the support of SEM observation.

References

[1] Strano G, Hao L, Everson RM, Evans KE. Surface roughness analysis, modelling and prediction in selective laser melting. J Mater Process Technol 2013;213:589–97.
[2] Yan C, Hao L, Hussein A, Raymont D. Evaluations of cellular lattice structures manufactured using selective laser melting. Int J Mach Tools Manuf 2012;62:32–8.
[3] Wang Y, Ren X, Chen Z, Jiang Y, Cao X, Fang S, Zhao T, Li Y, Fang D. Numerical and experimental studies on compressive behavior of gyroid lattice cylindrical shells. Mater Des 2020;186:108340.
[4] Qiu C, Adkins NJE, Attallah MM. Microstructure and tensile properties of selectively laser-melted and of HIPed laser-melted Ti-6Al-4V. Mater Sci Eng 2013;578:230–9.
[5] Uhlmann E, Kersting R, Klein TB, Cruz MF, Borille AV. Additive manufacturing of titanium alloy for aircraft components. Procedia Cirp 2015;35:55–60.
[6] Huang J, Yan X, Chang C, Xie Y, Ma W, Huang R, et al. Pure copper components fabricated by cold spray (CS) and selective laser melting (SLM) technology. Surf Coat Technol 2020;395:125936.
[7] Aboulkhair NT, Maskery I, Tuck C, Ashcroft I, Everitt NM. Improving the fatigue behaviour of a selectively laser melted aluminium alloy: influence of heat treatment and surface quality. Mater Des 2016;104:174–82.
[8] Lei H, Li C, Zhang X, Wang P, Zhou H, Zhao Z, et al. Deformation behavior of heterogeneous multi-morphology lattice core hybrid structures. Addit Manuf 2021;37:101674.
[9] Peng C, Tran P. Bioinspired functionally graded gyroid sandwich panel subjected to impulsive loadings. Compos Part B 2020;188:107773.
[10] Thijs L, Kempen K, Kruth J-P, Van Humbeeck J. Fine-structured aluminium products with controllable texture by selective laser melting of pre-alloyed AlSi10Mg powder. Acta Mater 2013;61(5):1809–19.
[11] Kok Y, Tan XP, Wang P, Nai M, Loh NH, Liu E, et al. Anisotropy and heterogeneity of microstructure and mechanical properties in metal additive manufacturing: a critical review. Mater Des 2018;139:565–86.
[12] Carroll BE, Palmer TA, Beese AM. Anisotropic tensile behavior of Ti-6Al-4V components fabricated with directed energy deposition additive manufacturing. Acta Mater 2015;87:309–20.
[13] Rodriguez OL, Allison PG, Whittington WR, Francis DK, Rivera OG, Chou K, et al. Dynamic tensile behavior of electron beam additive manufactured Ti-6Al-4V. Mater Sci Eng 2015;641:323–7.
[14] Clark D, Whittaker MT, Bache MR. Microstructural characterization of a prototype titanium alloy structure processed via direct laser deposition (DLD). Metall Mater Trans B 2012;43(2):388–96.
[15] Maconachie T, Leary M, Zhang J, Medvedev A, Sarker A, Ruan D, et al. Effect of build orientation on the quasi-static and dynamic response of SLM AlSi10Mg. Mater Sci Eng 2020:139445.
[16] Han Q, Gu H, Soe S, Setchi R, Lacan F, Hill J. Manufacturability of AlSi10Mg overhang structures fabricated by laser powder bed fusion. Mater Des 2018;160:1080–95.
[17] Schaedler TA, Carter WB. Architected cellular materials. Annu Rev Mater Res 2016;46:187–210.
[18] Comi C, Driemeier L. Wave propagation in cellular locally resonant metamaterials. Latin Am J Solids Struct 2018;15(4). https://doi.org/10.1590/1679-78254327.
[19] Jiang H, Ziegler H, Zhang Z, Meng H, Chronopoulos D, Chen Y. Mechanical properties of 3D printed architected polymer foams under large deformation. Mater Des 2020;194:108946.
[20] Maskery I, Aboulkhair NT, Aremu AO, Tuck CJ, Ashcroft IA. Compressive failure modes and energy absorption in additively manufactured double gyroid lattices. Addit Manuf 2017;16:24–9.
[21] Abueidda DW, Elhebeary M, Shiang C-SA, Pang S, Al-Rub RKA, Jasiuk IM. Mechanical properties of 3D printed polymeric gyroid cellular structures: experimental and finite element study. Mater Des 2019;165:107597.
[22] Schoen AH. Infinite periodic minimal surfaces without self-intersections. National Aeronautics and Space Administration; 1970.
[23] Yan C, Hao L, Hussein A, Young P, Raymont D. Advanced lightweight 316L stainless steel cellular lattice structures fabricated via selective laser melting. Mater Des 2014;55:533–41.
[24] Li X, Xiao L, Song W. Compressive behavior of selective laser melting printed gyroid structures under dynamic loading. Addit Manuf 2021;46:102054. https://doi.org/10.1016/j.addma.2021.102054.
[25] Novak N, Al-Ketan O, Krstulović-Opara L, Rowshan R, Al-Rub RKA, Vesenjak M, et al. Quasi-static and dynamic compressive behaviour of sheet TPMS cellular structures. Compos Struct 2021;266:113801.
[26] Abueidda DW, Bakir M, Al-Rub RKA, Bergström JS, Sobh NA, Jasiuk I. Mechanical properties of 3D printed polymeric cellular materials with triply periodic minimal surface architectures. Mater Des 2017;122:255–67.
[27] International A. Standard test methods for tension testing of metallic materials. ASTM international; 2016.
[28] Yang S-D, Lee HG, Kim J. A phase-field approach for minimizing the area of triply periodic surfaces with volume constraint. Comput Phys Commun 2010;181(6):1037–46.
[29] Santiago R, Cantwell W, Alves M. Impact on thermoplastic fibre-metal laminates: experimental observations. Compos Struct 2017;159:800–17.
[30] Kariem MA, Santiago RC, Govender R, Shu DW, Ruan D, Nurick G, et al. Round-Robin test of split Hopkinson pressure bar. Int J Impact Eng 2019;126:62–75.
[31] Alves M.. Impact engineering: fundamentals, experiments and nonlinear finite elements10.4322/978-85-455210-0-6. 2020.
[32] Santiago RC, Cantwell WJ, Jones N, Alves M. The modelling of impact loading on thermoplastic fibre-metal laminates. Compos Struct 2018;189:228–38.
[33] Johnson GR, Cook WH. A constitutive model and data for metals subjected to large strains, high strain rates and high temperatures. Proceedings of the 7th international symposium on ballistics, The Netherlands. vol. 21; 1983. p. 541–7.
[34] Murugesan M, Lee S, Kim D, Kang Y-H, Kim N. A comparative study of ductile damage models approaches for joint strength prediction in hot shear joining process. Procedia Eng 2017;207:1689–94.
[35] Segebade E, Gerstenmeyer M, Dietrich S, Zanger F, Schulze V. Influence of anisotropy of additively manufactured AlSi10Mg parts on chip formation during orthogonal cutting. Procedia CIRP 2019;82:113–8.
[36] Ferro P, Fabrizi A, Berto F, Savio G, Meneghello R, Rosso S. Defects as a root cause of fatigue weakening of additively manufactured AlSi10Mg components. Theor Appl Fract Mech 2020;108:102611.
[37] Lu C, Zhang C, Wen P, Chen F. Mechanical behavior of Al-Si10-Mg gyroid surface with variable topological parameters fabricated via laser powder bed fusion. J Mater Res Technol 2021;15:5650–7854. https://doi.org/10.1016/j.jmrt.2021.11.008.
[38] Gibson LJ, Ashby MF. Cellular solids: structure and properties. Cambridge University Press; 1999.
[39] Wang H, Tan D, Liu Z, Yin H, Wen G. On crashworthiness of novel porous structure based on composite TPMS structures. Eng Struct 2022;252:113640.
[40] Zhao M, Zhang DZ, Liu F, Li Z, Ma Z, Ren Z. Mechanical and energy absorption characteristics of additively manufactured functionally graded sheet lattice structures with minimal surfaces. Int J Mech Sci 2020;167:105262.
[41] Tascioglu E, Karabulut Y, Kaynak Y. Influence of heat treatment temperature on the microstructural, mechanical, and wear behavior of 316l stainless steel fabricated by laser powder bed additive manufacturing. Int J Adv Manuf Technol 2020;107:1947–56. https://doi.org/10.1007/s00170-020-04972-0.
[42] Brandl E, Heckenberger U, Holzinger V, Buchbinder D. Additive manufactured AlSi10Mg samples using selective laser melting (SLM): microstructure, high cycle fatigue, and fracture behavior. Mater Des 2012;34:159–69.
[43] Maskery I, Aboulkhair NT, Aremu AO, Tuck CJ, Ashcroft IA, Wildman RD, et al. A mechanical property evaluation of graded density Al-Si10-Mg lattice structures manufactured by selective laser melting. Mater Sci Eng 2016;670:264–74.
[44] Miralbés R, Ranz D, Higuera S. Study of the application of gyroid structures in cyclist helmets. International conference on the digital transformation in the graphic engineering. Springer; 2021. p. 64–70.
[45] Benzait Z, Trabzon L. A review of recent research on materials used in polymer–matrix composites for body armor application. J Compos Mater 2018;52(23):3241–63.